

Information Routing in Atomistic Foundation Models: How Task Alignment and Equivariance Shape Linear Disentanglement

Joshua Steier*
Independent Researcher

March 10, 2026

Abstract

What determines whether a molecular property prediction model organizes its representations so that geometric and compositional information can be cleanly separated? We introduce Compositional Probe Decomposition (CPD), which linearly projects out composition signal and measures how much geometric information remains accessible to a Ridge probe. We validate CPD with four independent checks, including a structural isomer benchmark where compositional projections score at chance while geometric residuals reach 94.6% pairwise classification accuracy.

Across ten models from five architectural families on QM9, we find a *linear accessibility gradient*: models differ by $6.6\times$ in geometric information accessible after composition removal (R_{geom}^2 from 0.081 to 0.533 for HOMO-LUMO gap). Three factors explain this gradient. Task alignment dominates: models trained on HOMO-LUMO gap (R_{geom}^2 0.44–0.53) outscore energy-trained models by $\sim 0.25 R^2$ regardless of architecture. Within-architecture ablations on two independent architectures confirm this: PaiNN drops from 0.53 to 0.31 when retrained on energy, and MACE drops from 0.44 to 0.08. Data diversity partially compensates for misaligned objectives, with MACE pretrained on MPTraj (0.36) outperforming QM9-only energy models.

Inside MACE’s representations, information routes by symmetry type: $L=1$ (vector) channels preferentially encode dipole moment ($R^2 = 0.59$ vs. 0.38 in $L=0$), while $L=0$ (scalar) channels encode HOMO-LUMO gap ($R^2 = 0.76$ vs. 0.34 in $L=1$). This pattern is absent in ViSNet. We also show that nonlinear probes produce misleading results on residualized representations, recovering $R^2 = 0.68$ –0.95 on a purely compositional target, and recommend linear probes for this setting.

1 Introduction

Atomistic foundation models such as MACE (Batatia et al., 2022), SchNet (Schütt et al., 2017), DimeNet++ (Klicpera et al., 2020), PaiNN (Schütt et al., 2021), and ViSNet (Wang et al., 2024) now predict molecular energies, forces, and electronic properties with accuracy approaching density functional theory at a fraction of the cost. As these models are deployed for virtual screening, catalyst design, and molecular dynamics, a basic question remains open: what do their intermediate representations encode, and how is that information organized? If a representation cleanly separates what a molecule is made of (its composition) from how those atoms are arranged (its geometry),

*Correspondence: joshuasteier@gmail.com

downstream tasks can selectively access the relevant signal. A model that entangles these factors forces every application to disentangle them from scratch.

Representational probing offers a natural way to answer this question: train a simple predictor on internal activations and measure what it recovers (Conneau et al., 2018; Hewitt & Manning, 2019; Alain & Bengio, 2017). But molecular properties reflect both composition and geometry, and these contributions are correlated. A probe on raw representations cannot distinguish genuine geometric encoding from compositional shortcuts. To isolate geometric signal, the composition contribution must first be removed.

We initially attempted this removal with Ridge regression and probed the residuals using gradient boosted trees (GBTs). The results were striking and wrong: on a purely compositional target (average atomic mass), GBT probes recovered $R^2 = 0.68\text{--}0.95$ from residuals that should contain no relevant signal. GBTs exploit high-dimensional residuals to reconstruct the projected-out signal, producing systematically inflated scores. This failure motivated both the methodological core of this paper and the exclusive use of linear probes for residualized representations.

We introduce Compositional Probe Decomposition (CPD), which fits an OLS projection to remove composition signal within each cross-validation fold, then probes the residual with Ridge regression to quantify linearly accessible geometric information. We validate CPD with four independent checks, including a structural isomer benchmark where compositional projections score at chance while geometric residuals reach 94.6% pairwise classification accuracy.

Applying CPD to ten models from five architectural families on QM9 (small organic molecules with up to 9 heavy atoms), we find a *linear accessibility gradient*: a $6.6\times$ spread in geometric information accessible after composition removal. This gradient is shaped by three interacting factors whose relative importance overturns a natural assumption in the field. Section 4.1 presents the gradient and decomposes it; Section 4.2 reveals structured information routing through MACE’s equivariant channels; and Section 4.3 demonstrates that nonlinear probes produce systematically inflated scores on residualized representations.

Contributions.

1. **CPD as a validated probing methodology**, including a structural isomer ground-truth test and evidence that nonlinear probes produce systematically inflated scores on residualized representations.
2. **A three-factor linear accessibility gradient** across ten models, showing task alignment ($\sim 0.25 R^2$ gap) dominates over equivariance and data diversity. Within-architecture ablations on two independent architectures (PaiNN: $\Delta = 0.223$; MACE: $\Delta = 0.338$) confirm that the training objective, not architecture, drives linear geometric accessibility.
3. **Information routing by irreducible representation** in MACE, where scalar and vector channels preferentially encode properties matching their symmetry type.
4. **Robustness across twelve checks**, with model rankings perfectly preserved (Spearman $\rho = 1.0$) under concept erasure, alternative composition features, partial regression, and isomer classification.

2 Background and Related Work

This work sits at the intersection of three lines of research: representational probing, equivariant neural networks for molecular modeling, and disentangled representation learning. We briefly review

each and identify the gap that CPD addresses.

2.1 Representational Probing

The idea of training a simple classifier or regressor on a neural network’s internal activations to understand what it has learned originates in natural language processing. Alain & Bengio (2017) trained linear classifiers on intermediate layers of deep networks to track how representations evolve with depth. Conneau et al. (2018) introduced a suite of “probing tasks” for sentence embeddings, measuring whether syntactic and semantic features could be recovered from fixed representations. Hewitt & Manning (2019) showed that syntactic tree distances are approximately encoded as linear maps in BERT’s embedding space, establishing that some language models organize structural information in a linearly accessible way.

A key methodological lesson from this literature is that probe complexity matters. Hewitt & Liang (2019) demonstrated that sufficiently expressive probes can achieve high accuracy even on random representations, and proposed control tasks to calibrate probe selectivity. We encounter an analogous problem in the molecular setting: gradient boosted tree probes recover high R^2 from residualized representations even when the target is purely compositional, precisely because their expressiveness allows them to reconstruct removed signal.

Probing has seen limited application in atomistic ML. Batatia et al. (2022b) analyzed MACE representations but did not separate composition from geometry. To our knowledge, no prior work has systematically probed molecular representations after removing the composition confound, which is the central methodological contribution of this paper.

2.2 Equivariant Architectures for Molecular Property Prediction

Neural networks for molecular property prediction have evolved along two axes: how they represent atomic environments and whether they respect physical symmetries. SchNet (Schütt et al., 2017) introduced continuous filter convolutions on interatomic distances, producing representations that are invariant to rotation and translation by construction. DimeNet++ (Klicpera et al., 2020) incorporated bond angles through directional message passing, adding sensitivity to local geometry while maintaining global invariance.

A second generation of models explicitly encodes equivariance, meaning their intermediate representations transform predictably under rotations. PaiNN (Schütt et al., 2021) maintains separate scalar and vector channels, where vector features rotate with the coordinate frame. MACE (Batatia et al., 2022) goes further, constructing messages using tensor products of spherical harmonics, which produces features that transform as irreducible representations of $SO(3)$ at multiple angular momentum orders ($L=0, 1, 2, \dots$). ViSNet (Wang et al., 2024) takes a different approach, using runtime geometric computations on scalar and vector features rather than explicit tensor product operations. ANI-2x (Devereux et al., 2020) uses handcrafted symmetry functions that are invariant by design, with no learned equivariant features.

A natural hypothesis is that models with richer equivariant structure produce representations where geometric information is more accessible. Our results partially support and partially refute this hypothesis: the relationship between equivariance and geometric accessibility depends critically on what the model was trained to predict.

2.3 Disentangled Representations

Disentangled representation learning seeks to produce latent spaces where distinct generative factors are encoded in separate dimensions or subspaces (Bengio et al., 2013; Higgins et al., 2017). Locatello

et al. (2019) showed that unsupervised disentanglement is impossible without inductive biases, motivating the study of which architectural and training choices encourage separation of factors. More recently, Huh et al. (2024) proposed the Platonic Representation Hypothesis: that models trained on different data and with different architectures converge toward a shared statistical model of reality. Our results complicate this picture. While all ten models encode both composition and geometry, they differ dramatically in *how* that information is organized, with task alignment and architecture interacting to produce qualitatively different representation structures.

In the molecular domain, the relevant factors are composition (which elements are present and in what proportions) and geometry (how those atoms are arranged in space). These factors are not independent: composition constrains the space of possible geometries, and many molecular properties correlate with both. This correlation is what makes naive probing misleading and what CPD is designed to address.

Our notion of disentanglement is specific and operational. We say a representation is *linearly disentangled* with respect to composition and geometry if, after linearly projecting out composition signal, a linear probe can still recover geometric information. This differs from the β -VAE tradition (Higgins et al., 2017) in that we measure accessibility of a known factor (geometry) after removal of another known factor (composition), rather than seeking to discover latent factors. It is closer in spirit to the concept erasure framework of Belrose et al. (2023), which finds the optimal linear guard against concept leakage. We use LEACE as one of our four validation checks and show that it produces rankings identical to CPD (Spearman $\rho = 1.0$ for three of four target properties).

2.4 Composition as a Confound in Molecular ML

The observation that composition alone is a strong predictor of molecular properties is well established. Matminer (Ward et al., 2018) and CrabNet (Wang et al., 2021) achieve competitive performance on materials property benchmarks using only compositional descriptors. On QM9, simple composition features (element fractions and atom count) explain roughly 39% of HOMO-LUMO gap variance and 87% of polarizability variance under linear regression.

This means that any model achieving high R^2 on these targets may be relying partly or entirely on composition. Probing studies that report high R^2 without controlling for composition cannot distinguish geometric encoding from compositional memorization. CPD addresses this directly by removing the linear composition subspace before probing, and the structural isomer benchmark provides a composition-free evaluation where only geometric information can contribute to prediction.

3 Methodology

We describe CPD in three parts: the composition features that define the signal to be removed (§3.1), the projection that removes it (§3.2), and the probing protocol that measures what remains (§3.3).

3.1 Composition Features

For each molecule, we construct a composition vector $\mathbf{z} \in \mathbb{R}^k$ encoding what elements are present and in what proportions. Our default specification uses $k = 6$ features: element fractions for C, H, N, O, and F (each divided by the total atom count), plus a standardized atom count (z-scored across the dataset). Because the element fractions sum to approximately one, all downstream regressions include an intercept term to avoid rank deficiency.

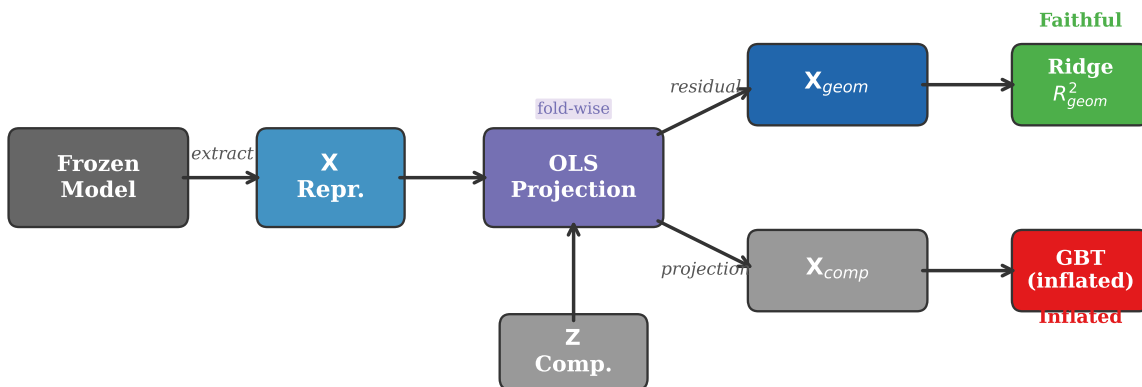


Figure 1: The CPD pipeline. Representations \mathbf{X} are extracted from a frozen model, then OLS projection (fold-wise) removes the linear composition component $\mathbf{Z}\hat{\beta}$, producing a geometric residual \mathbf{X}_{geom} . Ridge regression on the residual yields R_{geom}^2 (faithful). Gradient boosted trees on the same residual produce inflated scores by reconstructing the projected-out composition signal.

A natural concern is that results might depend on how composition is defined. We test this by repeating all analyses under three alternative specifications: raw element counts with raw atom count (unnormalized), element fractions without atom count, and binary element presence indicators with standardized atom count. Section 5 shows the model ranking is invariant to this choice (Spearman $\rho = 1.0$ across all pairwise comparisons).

3.2 Compositional Probe Decomposition

Let $\mathbf{X} \in \mathbb{R}^{n \times d}$ be the matrix of molecular representations extracted from a frozen model, and let $\mathbf{Z} \in \mathbb{R}^{n \times k}$ be the corresponding composition feature matrix. CPD removes the linear relationship between composition and representation by fitting an ordinary least squares regression of \mathbf{X} on \mathbf{Z} and taking the residual:

$$\hat{\beta} = (\mathbf{Z}^\top \mathbf{Z})^{-1} \mathbf{Z}^\top \mathbf{X}, \quad \mathbf{X}_{\text{geom}} = \mathbf{X} - \mathbf{Z}\hat{\beta}. \quad (1)$$

The residual \mathbf{X}_{geom} is the component of the representation that is linearly orthogonal to composition. The compositional component is $\mathbf{X}_{\text{comp}} = \mathbf{Z}\hat{\beta}$.

This operation is equivalent to QR projection: computing $\mathbf{Q}, \mathbf{R} = \text{qr}(\mathbf{Z})$ and setting $\mathbf{X}_{\text{geom}} = \mathbf{X} - \mathbf{Q}\mathbf{Q}^\top \mathbf{X}$. We use the OLS formulation because it extends naturally to the fold-wise setting described below. Figure 1 illustrates the full CPD pipeline.

Fold-wise projection. Computing $\hat{\beta}$ on the full dataset and then evaluating probes under cross-validation introduces a subtle information leak: the projection coefficients are informed by test-fold composition vectors. While the leak is small for low-dimensional \mathbf{Z} ($k = 6$), we eliminate it entirely by fitting $\hat{\beta}$ on training data only within each fold and applying the resulting projection to both train and test splits. This is equivalent to the Frisch-Waugh-Lovell theorem applied fold-wise, and it ensures that the test-fold residuals are computed from a projection the model has not seen. In practice, fold-wise CPD produces slightly higher R_{geom}^2 values than global CPD (mean $\Delta = +0.04$), because global projection removes a wider subspace. The model ranking is identical under both approaches.

What the residual contains. We use the notation R_{geom}^2 for readability, but the residual \mathbf{X}_{geom} is not purely three-dimensional geometry. It captures all information that is linearly independent of composition, including molecular topology, bond connectivity, conformational features, and any nonlinear interactions between composition and structure. We use “non-compositional signal” and “geometric information” interchangeably throughout, with the understanding that the latter is a convenient shorthand for the former.

3.3 Probing Protocol

We extract molecular representations from each frozen, pretrained model by passing a fixed set of 2,000 QM9 molecules through the network and saving the final-layer activations as mean-pooled per-molecule vectors. The 2,000 molecules are selected by a fixed random permutation (seed 42) to ensure identical evaluation sets across all models.

For each model, we train Ridge regression probes (`RidgeCV` with 20 log-spaced regularization values from 10^{-3} to 10^6 , `fit_intercept=True`) on four targets: HOMO-LUMO gap, dipole moment, polarizability, and zero-point vibrational energy (ZPVE). All results use 5-fold cross-validation repeated across 30 random seeds, with reported values being the mean $R^2 \pm$ standard deviation across seeds.

Why linear probes. A central finding of this paper is that nonlinear probes produce misleading results on residualized representations. Gradient boosted trees recover $R^2 = 0.68\text{--}0.95$ on average atomic mass (a purely compositional target) from \mathbf{X}_{geom} , which should contain no compositional signal. This inflation occurs because GBTs have enough capacity to reconstruct the projected-out composition signal from high-dimensional residuals through nonlinear feature interactions. Linear probes cannot perform this reconstruction and therefore provide a faithful measure of what is linearly accessible in the residual. We report GBT results only as a cautionary comparison.

3.4 Models

We evaluate ten models spanning five architectural families (Table 1). The models differ in three dimensions that our analysis aims to disentangle: equivariant structure, training objective, and training data.

PaiNN, ViSNet, and MACE-HL are trained on HOMO-LUMO gap, the same property we use as our primary probe target. This is deliberate: it allows us to test whether task alignment between training and probing objectives affects disentanglement. PaiNN-energy uses identical architecture to PaiNN but is trained on QM9 energy (U_0), and MACE-HL uses identical architecture to the MACE QM9 variants but is trained on HOMO-LUMO gap. Together these provide two independent within-architecture ablations of training objective. The remaining models are all trained on energy-related objectives, providing a within-objective comparison group where architecture and data vary but the training target does not.

The MACE family provides a controlled ablation. MACE pretrained, MACE QM9 97ep, and MACE QM9 30ep share identical architecture (ScaleShiftMACE, 128 scalar + 128 vector channels, $\ell_{\text{max}} = 2$, correlation order 3) but differ in training data and duration. Any difference in their R_{geom}^2 scores is attributable to training rather than architecture. Parameter counts range from 0.46M (SchNet) to 13.7M (ANI-2x) with no correlation to R_{geom}^2 : ANI-2x (13.7M) scores 0.331, while PaiNN ($12\times$ smaller, 1.17M) scores 0.533. This rules out model capacity as a confound for the gradient.

Table 1: Models evaluated. “Equiv.” indicates whether the architecture produces equivariant intermediate representations. “TP” indicates tensor product message passing. PaiNN and MACE each appear in both HOMO-LUMO and energy-trained variants, enabling two independent 2×2 factorial tests of task alignment.

Model	Equiv.	TP	Params	Training Objective	Training Data
PaiNN	✓	×	1.17M	HL gap	QM9 (30 ep)
ViSNet	✓	×	1.67M	HL gap	QM9 (50 ep)
MACE-HL	✓	✓	0.73M	HL gap	QM9 (30 ep)
MACE pretrained	✓	✓	3.70M*	E + F	MPTraj (millions)
ANI-2x	×	×	13.7M	E	ANI-1x (diverse)
PaiNN-energy	✓	×	1.17M	E (U_0)	QM9 (30 ep)
SchNet	×	×	0.46M	E (U_0)	QM9 (30 ep)
DimeNet++	×	×	1.89M	E (U_0)	QM9 (30 ep)
MACE QM9 97ep	✓	✓	0.73M	E	QM9 (97 ep)
MACE QM9 30ep	✓	✓	0.73M	E	QM9 (30 ep)

*Published value for MACE-MP-0-medium.

Limitations of the model set. DimeNet++ was trained for only 30 epochs and achieves the lowest R_{full}^2 (0.617), suggesting it may not have fully converged. Its position on the gradient should be interpreted with this caveat. We also note that our QM9 model set covers small organic molecules with up to 9 heavy atoms; the Materials Project extension (Section 4.6) broadens coverage to periodic crystals. We discuss remaining scope limitations in Section 7.

3.5 Irreducible Representation Analysis

MACE’s equivariant architecture produces representations that decompose into channels transforming as irreducible representations of $\text{SO}(3)$. At each layer, the output contains scalar ($L=0$) features that are invariant under rotation and vector ($L=1$) features that rotate with the molecular frame. This decomposition allows us to ask whether the model routes different types of information through different symmetry channels.

We extract $L=0$ and $L=1$ channels separately from MACE’s final interaction layer. The $L=1$ channels are three-dimensional vectors; to probe them for scalar properties, we convert them to invariant features by computing the norm (magnitude) of each vector. We then run the standard CPD and Ridge probing pipeline independently on each channel type.

For comparison, we perform the same analysis on ViSNet, which also maintains scalar and vector feature streams but constructs them through runtime geometric operations rather than tensor products. If information routing is a general property of equivariant architectures, both models should show similar channel specialization. If it is specific to tensor product message passing, the pattern should appear in MACE but not ViSNet.

3.6 Structural Isomer Benchmark

The strongest test of whether CPD successfully separates composition from geometry is to evaluate it on molecules that share identical composition. Structural isomers have the same molecular formula but different atomic arrangements, so any difference in their properties is entirely geometric.

Within our 2,000-molecule probe set, we identify 150 isomer groups containing 1,931 molecules and forming 38,784 isomer pairs. For each pair (i, j) of isomers, we compute the signed representation difference $\mathbf{X}[i] - \mathbf{X}[j]$ and train a logistic regression classifier (5-fold CV) to predict which

Table 2: Fold-wise CPD results on HOMO-LUMO gap. All values are mean $R^2 \pm$ standard deviation across 30 seeds \times 5 folds. Models are ordered by R_{geom}^2 .

Model	Equiv.	Target	R_{full}^2	R_{geom}^2	R_{comp}^2
PaiNN	✓	HL gap	0.949	0.533 ± 0.004	0.389
ViSNet	✓	HL gap	0.877	0.513 ± 0.010	0.389
MACE-HL	✓	HL gap	0.715	0.439 ± 0.005	0.389
MACE pretrained	✓	Energy	0.786	0.364 ± 0.007	0.389
ANI-2x	×	Energy	0.771	0.331 ± 0.006	0.389
PaiNN-energy	✓	Energy	0.656	0.310 ± 0.005	0.389
SchNet	×	Energy	0.692	0.262 ± 0.012	0.389
DimeNet++	×	Energy	0.617	0.240 ± 0.005	0.389
MACE QM9 97ep	✓	Energy	0.289	0.101 ± 0.004	0.335 [†]
MACE QM9 30ep	✓	Energy	0.342	0.081 ± 0.004	0.389

[†]See footnote 1.

molecule has the higher HOMO-LUMO gap.

This benchmark has a built-in control: since isomers share identical composition vectors, the compositional component \mathbf{X}_{comp} must produce the same vector for both molecules, and classification accuracy must be at chance (50%). Any accuracy above chance in \mathbf{X}_{geom} is direct evidence that the geometric residual carries structural information that composition cannot explain.

4 Results

We organize our results around three findings: the linear accessibility gradient and the three factors that shape it (§4.1), information routing through MACE’s equivariant channels (§4.2), and systematic inflation from nonlinear probes (§4.3). Robustness analyses appear in Section 5.

4.1 The Linear Accessibility Gradient

Table 2 presents the main result. After removing composition signal via fold-wise CPD, models differ by a factor of $6.6\times$ in how much geometric information remains linearly accessible. PaiNN achieves the highest score ($R_{\text{geom}}^2 = 0.533$) and MACE QM9 30ep the lowest (0.081). The compositional component R_{comp}^2 is approximately constant across models (≈ 0.39 for HOMO-LUMO gap), confirming that it reflects the dataset-level correlation between composition and property rather than anything model-specific.¹

The gradient is shaped by three interacting factors, which we now examine. Figure 2 visualizes the full gradient with models color-coded by training objective.

4.1.1 Factor 1: Task Alignment Dominates

The clearest pattern in Table 2 is a gap between models trained on HOMO-LUMO gap and models trained on energy. PaiNN, ViSNet, and MACE-HL (R_{geom}^2 of 0.533, 0.513, and 0.439 respectively) outscore every energy-trained model by at least $0.07 R^2$, and the gap reaches 0.35 when compared

¹MACE QM9 97ep shows a slightly lower R_{comp}^2 (0.335) because its representation space is lower quality overall: the Ridge probe’s regularization interacts differently with a less informative embedding. The composition features \mathbf{Z} are identical across models; only the representation \mathbf{X} differs.

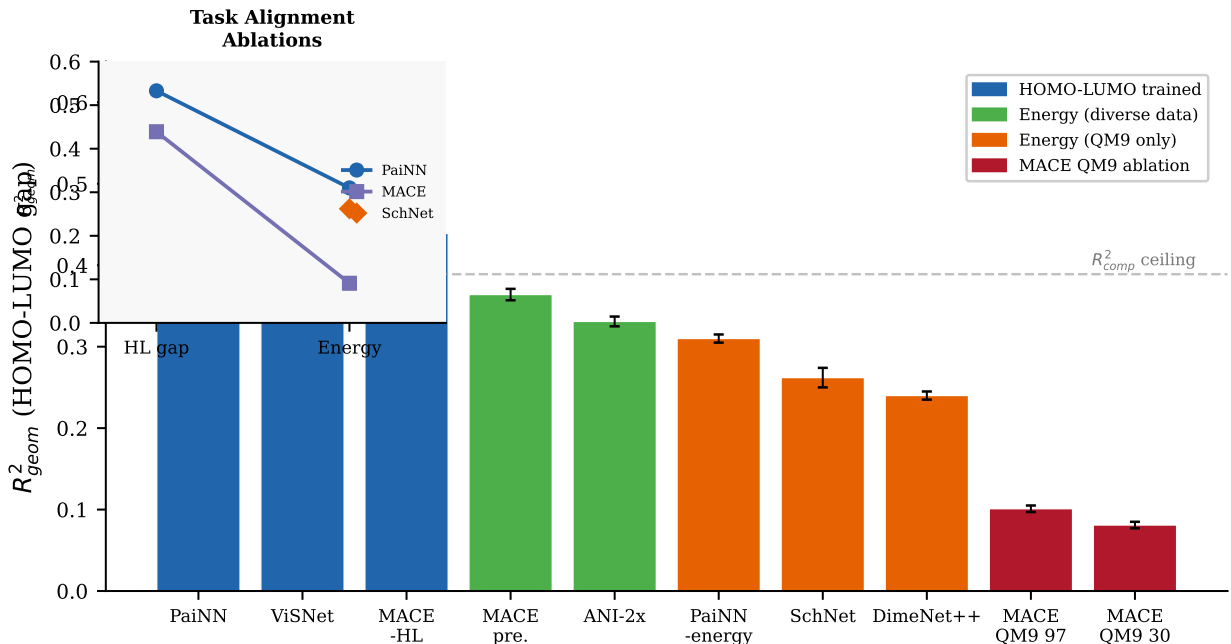


Figure 2: The linear accessibility gradient. R^2_{geom} for HOMO-LUMO gap across ten models, color-coded by training regime. Three clusters emerge: HOMO-LUMO-trained (blue), energy-trained with diverse data (green), and energy-trained on QM9 only (orange/red). Inset: the 2×2 factorial crossing PaiNN’s architecture with training objective, showing the task alignment effect ($\Delta = 0.223$) is $4.6\times$ larger than the architecture effect ($\Delta = 0.048$). Dashed line shows the composition R^2 ceiling.

to the energy-trained MACE QM9 variants. This holds regardless of whether the architecture uses tensor products.²

The interpretation follows directly. HOMO-LUMO gap is sensitive to molecular geometry (orbital symmetry, conjugation patterns, steric effects), so models trained on it are forced to develop representations where geometric signal is prominent. Models trained on total energy face a different incentive: energy is dominated by composition, with geometry contributing a smaller correction. Their representations reflect this balance.

Table 3 extends this analysis to four properties. The task-alignment effect is strongest for HOMO-LUMO gap and dipole moment, where the geometric contribution is large relative to the compositional floor. For polarizability ($R^2_{\text{comp}} = 0.87$), the composition ceiling leaves little variance for geometry to explain, and the gradient compresses accordingly. The PaiNN ablation reveals that task alignment is property-specific: switching from HOMO-LUMO to energy training drops R^2_{geom} for HL gap by 0.223 but *increases* it for ZPVE by 0.060, because ZPVE correlates more strongly with total energy. The training objective reshapes which geometric information is linearly accessible, not just how much.

²MACE-HL’s lower R^2_{full} (0.715 vs. PaiNN’s 0.949) suggests that the MACE architecture is less sample-efficient at learning HOMO-LUMO gap from QM9 at 30 epochs, which may suppress its R^2_{geom} relative to its ceiling. The rank ordering within the HL-trained group (PaiNN > ViSNet > MACE-HL) may partly reflect differences in prediction quality rather than pure representation organization.

Table 3: R_{geom}^2 across four QM9 properties (fold-wise CPD, 30-seed). PaiNN-HL and PaiNN-energy (PaiNN-E) show how task alignment reshapes geometric accessibility across properties: HOMO-LUMO gap drops by 0.223 when switching to energy training, while ZPVE increases by 0.060. Bottom row shows the composition R^2 ceiling.

Model	HL Gap	Dipole	Polariz.	ZPVE
PaiNN	0.533	0.171	0.051	0.188
PaiNN-energy	0.310	0.201	0.081	0.248
ViSNet	0.513	0.141	0.056	0.190
MACE-HL	0.439	0.144	0.068	0.175
MACE pretrained	0.364	0.298	0.060	0.247
ANI-2x	0.331	0.266	0.063	0.247
SchNet	0.262	0.243	0.073	0.243
DimeNet++	0.240	0.201	0.074	0.224
MACE QM9 97ep	0.101	0.053	0.028	0.129
R_{comp}^2	0.389	0.199	0.868	0.702

4.1.2 Factor 2: Equivariance Amplifies but Cannot Substitute

A natural expectation is that equivariant architectures should produce higher geometric accessibility. Our results show this is conditionally true.

Within the HOMO-LUMO-trained group, PaiNN and ViSNet sit at the top of the gradient. But within the energy-trained group, equivariance does not help. MACE QM9 30ep (equivariant) scores 0.081, well below invariant SchNet (0.262) and DimeNet++ (0.240). This is the most counterintuitive result in the paper: an equivariant tensor product model, trained on the wrong objective, produces representations where geometric information is *less* linearly accessible than in simpler invariant models.

The MACE architecture ablation makes this concrete. MACE pretrained (0.364), MACE QM9 97ep (0.101), and MACE QM9 30ep (0.081) share identical architecture. The $4.5\times$ gap between pretrained and 30ep is direct evidence that training conditions, not tensor product message passing, determine MACE’s position on the gradient. PaiNN reinforces this point from the opposite direction: it achieves the highest R_{geom}^2 in our study (0.533) using equivariant message passing *without* tensor products, demonstrating that tensor products are not necessary for high geometric accessibility. The critical combination is equivariance plus a task-aligned training signal.

Two independent within-architecture ablations provide causal tests of task alignment. PaiNN and PaiNN-energy share identical architecture (6 layers, 128 hidden, 1.17M parameters) but differ only in training objective. MACE-HL and the MACE QM9 variants share identical architecture (ScaleShiftMACE, 0.73M parameters) but differ only in training objective.³ This yields a 2×2 factorial replicated across two architectures:

	HL-trained	Energy-trained	Task Δ
PaiNN (equiv, no TP)	0.533	0.310	+0.223
MACE (equiv, TP)	0.439	0.081–0.101	+0.338–0.358
SchNet (invariant)	—	0.262	—

Task alignment dominates in both architectures. For PaiNN, the task effect ($\Delta = 0.223$) is $4.6\times$

³MACE-HL was trained for 30 epochs on QM9 HOMO-LUMO gap, achieving test RMSE 25.8 meV. See Appendix C.

Table 4: Information routing in MACE pretrained. Bold indicates the dominant channel for each property. MACE routes scalar properties through $L=0$ and vector properties through $L=1$. Wilcoxon signed-rank test confirms the dipole preference for $L=1$ ($p = 1.86 \times 10^{-9}$, 30 seeds).

Channel	HL Gap R^2	Dipole R^2
Full representation	0.786	0.499
$L=0$ (scalar)	0.756	0.379
$L=1$ (vector norm)	0.337	0.586

larger than the architecture effect (PaiNN-energy vs. SchNet, $\Delta = 0.048$). For MACE, the task effect is even larger ($\Delta = 0.338-0.358$). That task alignment replicates independently across two architectures with different equivariant mechanisms (vector channels vs. tensor products) is strong evidence that the training objective, not architecture, is the primary determinant of linear geometric accessibility.

4.1.3 Factor 3: Data Diversity Compensates

Among the energy-trained models, a secondary gradient tracks training data diversity. MACE pretrained (0.364, MPTraj, millions of structures) and ANI-2x (0.331, ANI-1x, diverse conformations) both outperform SchNet (0.262) and DimeNet++ (0.240), which were trained on QM9 alone.

The most informative comparison is MACE pretrained (0.364) versus MACE QM9 97ep (0.101) on identical architecture. The $3.6\times$ gap, with only training data differing, suggests that exposure to diverse chemical environments encourages representations that make geometric information accessible even for properties the model was not trained to predict.

This compensation is partial. Even with massive pretraining diversity, MACE pretrained (0.364) does not reach the task-aligned cluster (PaiNN/ViSNet at ≈ 0.52). Data diversity narrows the gap but does not close it.

4.2 Information Routing by Irreducible Representation

MACE’s equivariant architecture produces representations with channels transforming as irreducible representations of $SO(3)$. We test whether different types of information are routed through channels matching their physical symmetry by probing $L=0$ (scalar) and $L=1$ (vector, norm-converted to invariant features) channels independently.

Table 4 shows the result. Scalar channels carry most of the HOMO-LUMO gap information ($R^2 = 0.756$, close to the full representation at 0.786), while vector channels dominate for dipole moment ($R^2 = 0.586$ vs. 0.379 in $L=0$; Wilcoxon $p = 1.86 \times 10^{-9}$). MACE has learned to route scalar properties through scalar channels and vector properties through vector channels.

For comparison, we probe ViSNet’s scalar and vector streams independently on HOMO-LUMO gap. ViSNet concentrates virtually all linearly accessible information in its scalar stream ($R^2 = 0.877$), while the vector stream carries almost nothing ($R^2 = 0.018$). This suggests that ViSNet’s equivariant operations contribute through internal computation during message passing rather than through persistent structure in the output. The routing pattern is not a generic consequence of equivariance but appears specific to architectures that maintain explicit irreducible representation channels through to the output layer. Figure 3 visualizes this contrast.

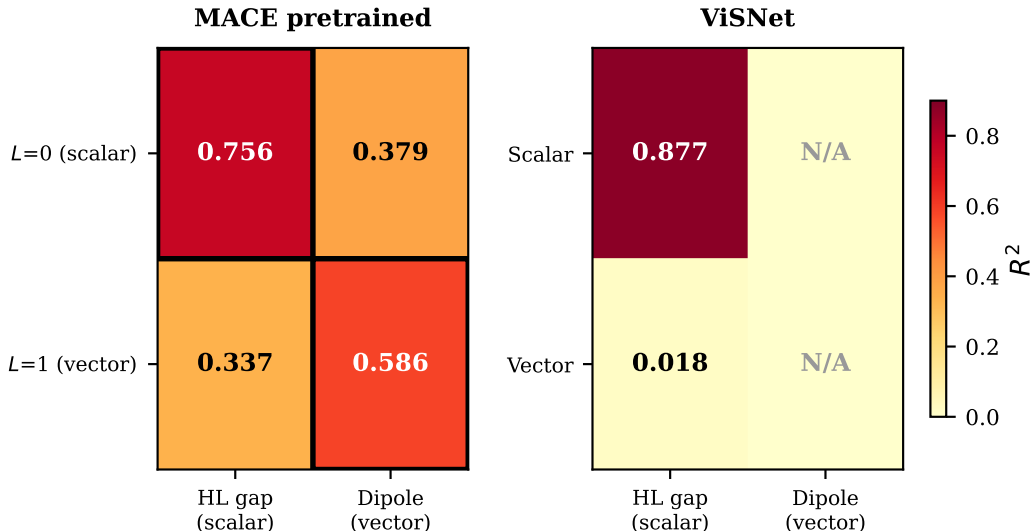


Figure 3: Information routing by symmetry channel. Left: MACE routes scalar properties (HL gap) through $L=0$ channels and vector properties (dipole) through $L=1$ channels (black boxes highlight the dominant diagonal). Right: ViSNet concentrates all information in its scalar stream; vector channels carry $R^2 = 0.018$.

Table 5: Probe comparison on average atomic mass (purely compositional). Ridge correctly returns ≈ 0 . GBTs produce inflated scores.

Model	Ridge	GBT
MACE pretrained	-0.003	0.95
ViSNet	-0.003	0.89
ANI-2x	-0.002	0.93
SchNet	-0.003	0.85
DimeNet++	-0.003	0.68
MACE QM9	-0.003	0.71

4.3 Nonlinear Probe Inflation

We motivate the exclusive use of linear probes with a controlled experiment. We compute R_{geom}^2 using both Ridge regression and gradient boosted trees on average atomic mass, a purely compositional target. \mathbf{X}_{geom} should contain no relevant signal, so a well-behaved probe should return $R^2 \approx 0$.

Ridge behaves as expected ($R_{\text{geom}}^2 \approx -0.003$ across all models). GBTs recover $R^2 = 0.68$ to 0.95 from the same residuals (Table 5). The explanation is that OLS projection removes only the *linear* composition component; the residual retains nonlinear functions of composition that a tree ensemble can exploit to reconstruct the projected-out target. Linear probes cannot perform this reconstruction and therefore provide a faithful measure of what is linearly accessible.

This finding generalizes: any probing study that applies nonlinear probes to residualized or concept-erased representations risks the same inflation. We recommend linear probes as the primary metric for residualization-based probing. Figure 4 visualizes the contrast.

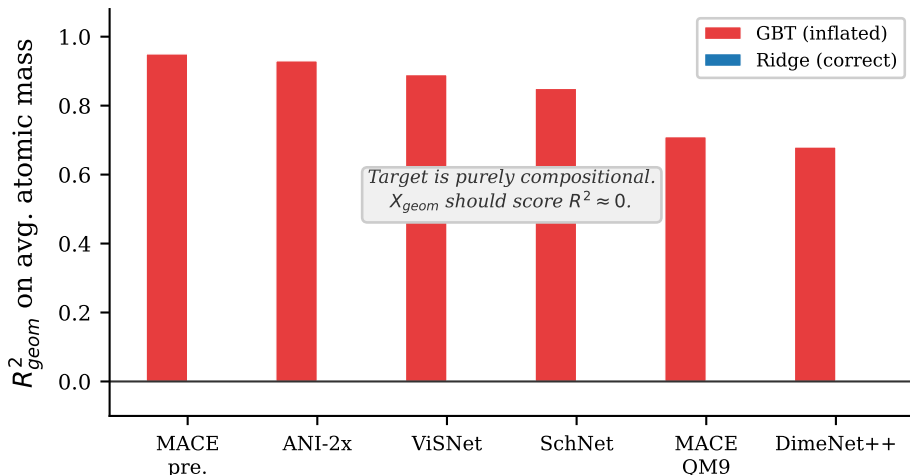


Figure 4: GBT inflation on a purely compositional target (average atomic mass). Ridge regression correctly returns $R^2 \approx 0$ on the geometric residual (blue). Gradient boosted trees recover $R^2 = 0.68\text{--}0.95$ from the same residuals (red) by reconstructing the projected-out composition signal through nonlinear feature interactions.

Table 6: Structural isomer ordering accuracy (38,784 pairs, logistic regression, 5-fold CV). \mathbf{X}_{comp} scores at chance by construction.

Model	\mathbf{X}_{geom}	\mathbf{X}_{comp}
PaiNN	94.6% \pm 0.1	52.5% \pm 0.5
ViSNet	88.1% \pm 0.4	52.5% \pm 0.5
ANI-2x	87.6% \pm 0.2	52.5% \pm 0.5
MACE pretrained	84.3% \pm 0.3	52.5% \pm 0.5
DimeNet++	78.3% \pm 0.5	52.5% \pm 0.5
SchNet	78.1% \pm 0.5	52.5% \pm 0.5
MACE QM9	66.5% \pm 1.3	52.5% \pm 0.5

4.4 Structural Isomer Validation

Among molecules with identical composition, can the geometric residual distinguish structural differences while the compositional component cannot? Table 6 shows the answer. The compositional component produces 52.5% accuracy for every model, exactly at chance since isomers share the same formula. The geometric residual ranges from 66.5% (MACE QM9) to 94.6% (PaiNN), tracking the R^2_{geom} ranking from the regression analysis.

PaiNN’s 94.6% means its geometric residual correctly orders the HOMO-LUMO gap of same-formula molecules 19 times out of 20 under a simple logistic regression probe. This confirms that CPD preserves rich structural information while genuinely removing composition (Figure 5). It also validates the gradient through a completely different evaluation paradigm: pairwise classification within fixed compositions rather than regression R^2 over a mixed-composition sample. Both paradigms produce the same model ranking.

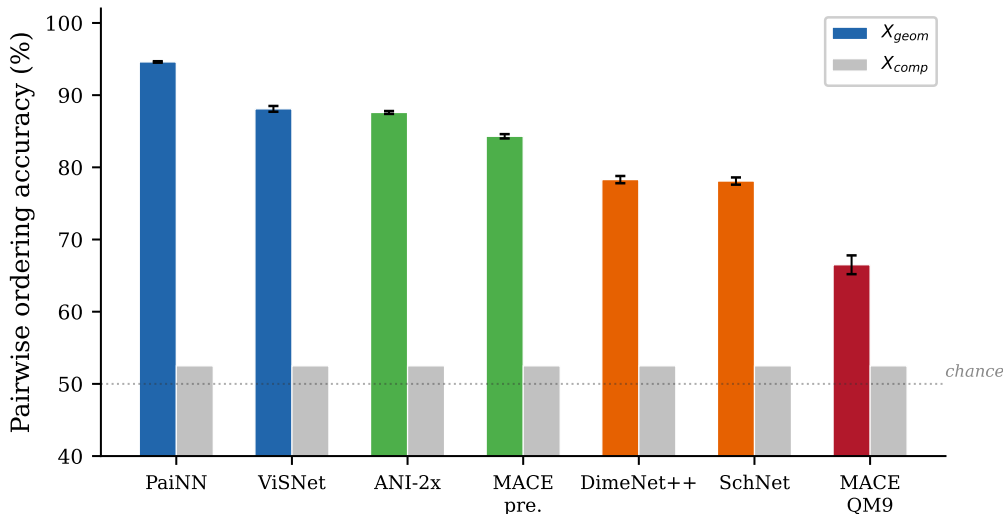


Figure 5: Structural isomer ordering accuracy (38,784 pairs). For each model, the geometric residual (colored bars) distinguishes isomers well above chance, while the compositional component (gray bars) scores exactly at 52.5% for every model, as required since isomers share identical formulas. PaiNN’s 94.6% means correct ordering 19 out of 20 times.

4.5 Sample Efficiency

If the linear accessibility gradient is a structural property of representations rather than a statistical artifact, it should emerge even at small sample sizes. We test this by computing R_{geom}^2 at $N = 50, 100, 200, 500, 1,000,$ and $2,000$ for all models.

The gradient is stable across sample sizes. At $N = 50$, the model ranking already achieves Spearman $\rho = 0.964$ with the full-sample ranking. By $N = 500$, it is perfect ($\rho = 1.000$). PaiNN and ViSNet separate from the energy-trained cluster immediately: at $N = 50$, both show $R_{geom}^2 > 0.13$ while all energy-trained models produce negative R^2 (indicating worse-than-baseline prediction at this sample size).

The practical implication is striking. PaiNN at $N = 50$ ($R_{geom}^2 = 0.296$) already exceeds SchNet at $N = 2,000$ (0.262). Linearly disentangled representations require dramatically fewer labeled examples to extract geometric signal, suggesting that representation organization matters at least as much as sample size for downstream probing tasks (Figure 6).

4.6 Extension to Materials Project Crystals

To test whether the findings above generalize beyond small organic molecules, we apply CPD to three models trained on the Materials Project crystal dataset: MACE (pretrained), SevenNet, and CHGNet. We probe five properties spanning electronic (band gap, is_metal), thermodynamic (formation energy), and structural (density, volume per atom) targets across all available layers of each model.

Table 7 shows the best-layer R^2 for each model-property pair. The composition-geometry separation observed on QM9 replicates on crystals: band gap and formation energy have the largest geometric contributions ($\Delta_{best} \approx 0.19$ above the composition baseline), while density, volume, and is_metal are composition-dominated ($\Delta < 0.05$). This mirrors the variance budget relationship from Equation 2: properties with lower composition ceilings allow wider gradients.

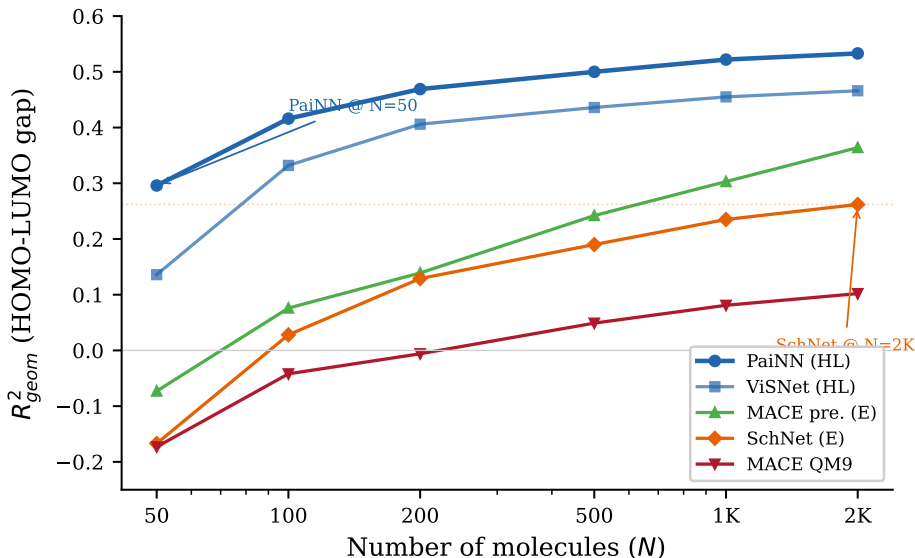


Figure 6: Sample efficiency of the linear accessibility gradient. The gradient emerges at $N = 50$ (Spearman $\rho = 0.964$) and stabilizes by $N = 500$ ($\rho = 1.0$). PaiNN at $N = 50$ ($R^2_{\text{geom}} = 0.296$) already exceeds SchNet at $N = 2,000$ (0.262), demonstrating that linearly disentangled representations are dramatically more sample-efficient.

Table 7: Materials Project crystals: best-layer R^2 per model and property. Baseline is linear regression on composition features alone. Δ_{best} is the improvement of the best model over the composition baseline.

Property	Baseline	MACE	SevenNet	CHGNet	Δ_{best}
Band gap	0.530	0.723	0.669	0.666	+0.193
Formation E	0.789	0.986	0.953	0.926	+0.197
Is_metal (clf)	0.889	0.897	0.895	0.899	+0.010
Density	0.922	0.954	0.931	0.935	+0.032
Vol./atom	0.924	0.968	0.968	0.960	+0.044

The per-layer depth profiles reveal architectural differences in how geometric information builds through the network. MACE’s R^2_{geom} increases monotonically from early interaction layers to `descriptors_final` for all properties, consistent with progressive refinement of geometric representations. SevenNet peaks at intermediate layers (`conv_1` or `conv_2`) and then *decreases* through deeper layers, suggesting information loss in late message-passing steps. CHGNet shows property-dependent depth profiles: density peaks at `conv_0` (early layers capture packing geometry) while formation energy increases monotonically through `conv_3`.

MACE leads on four of five properties, consistent with its position atop the QM9 energy-trained gradient. The key finding is that the composition-geometry separation and the variance budget relationship both transfer from small organic molecules to periodic crystals, supporting the generality of the CPD framework and the three-factor narrative beyond a single dataset.

We now test whether these rankings hold under alternative methodological choices.

Table 8: Consolidated robustness summary. Spearman ρ is computed between the default model ranking and the ranking under each alternative. All checks preserve the gradient.

Robustness Check	Spearman ρ	Section
Fold-wise vs. global CPD	1.000	5.1
FWL partial R^2	0.943*	5.2
Z1 vs. Z2 (raw counts)	1.000	5.3
Z1 vs. Z3 (fractions only)	1.000	5.3
Z1 vs. Z4 (binary presence)	1.000	5.3
CPD vs. LEACE (HL gap)	1.000	5.4
CPD vs. LEACE (dipole)	1.000	5.4
CPD vs. LEACE (polarizability)	1.000	5.4
Random subspace control	$z < -163$	5.5
GBT inflation control	N/A	4.3
PCA dimensionality matching	Preserved	5.6
Isomer classification	Tracks R^2	4.4

*One adjacent swap (ANI-2x and MACE pretrained, positions 2/3), within error bars.

5 Robustness and Validation

The linear accessibility gradient could reflect a methodological artifact rather than a genuine property of the representations. The model ranking might depend on how composition features are defined, on whether the projection leaks information across cross-validation folds, or on whether OLS is too weak an eraser. We test each of these possibilities. Table 8 summarizes all twelve checks; we describe the key experiments below. Full per-model numbers for every check appear in Appendix A.

5.1 Fold-Wise vs. Global Projection

As described in Section 3.2, global CPD computes the projection matrix using all samples including the test fold, introducing a potential information leak. We compare global and fold-wise R_{geom}^2 for all models.

Fold-wise values are consistently higher (mean $\Delta = +0.04$), because global QR projects out a wider subspace informed by test-fold composition vectors, over-removing geometric signal. The effect is largest for ViSNet ($\Delta = +0.069$) and smallest for MACE QM9 ($\Delta = +0.011$). The model ranking is identical under both approaches (Spearman $\rho = 1.0$). All results reported in this paper use fold-wise CPD. Per-model values for both methods appear in Table 9.

5.2 Frisch-Waugh-Lovell Partial R^2

Standard CPD residualizes the representation \mathbf{X} but not the target y . The Frisch-Waugh-Lovell (FWL) theorem shows that regressing residualized y on residualized \mathbf{X} yields the same regression coefficients as including \mathbf{Z} as a covariate. The resulting partial R^2 measures what fraction of *non-compositional* target variance the geometric residual explains, using a different denominator than our standard R_{geom}^2 .

Under FWL, absolute values increase substantially (ViSNet reaches 0.826, meaning 83% of non-compositional HOMO-LUMO gap variance is captured) because the denominator excludes composition variance. The ranking is preserved with one adjacent swap: ANI-2x (0.691) and MACE pretrained (0.644) exchange positions 2 and 3, a difference well within their respective error

bars (Spearman $\rho = 0.943$). MACE QM9 remains at the bottom (0.167), confirming the gradient under an independent statistical framework (Table 10).

5.3 Composition Feature Sensitivity

The default composition vector \mathbf{Z} uses element fractions and standardized atom count. To ensure the gradient is not an artifact of this particular choice, we repeat the full analysis under three alternatives: raw element counts with raw atom count (Z2), element fractions without atom count (Z3), and binary element presence with standardized atom count (Z4).

The model ranking is perfectly preserved under all four specifications (Spearman $\rho = 1.0$ for all six pairwise comparisons). Absolute values shift: Z4 (binary presence) is the most conservative specification, removing less composition signal and producing higher R_{geom}^2 across the board. Z2 (raw counts) removes the most and produces lower values. But in every case, PaiNN and ViSNet lead, MACE QM9 trails, and the ordering between them is unchanged (Table 11).

5.4 LEACE Concept Erasure

LEACE (Belrose et al., 2023) finds the theoretically optimal linear projection for removing a concept from a representation. If CPD’s simpler OLS projection captures the same composition subspace as the optimal eraser, their rankings should agree. If they disagree, CPD may be leaving composition signal in the residual or removing non-compositional signal.

Rankings are identical (Spearman $\rho = 1.0$) for HOMO-LUMO gap, dipole moment, and polarizability, with mean absolute R^2 difference of 0.012 for HOMO-LUMO gap (Table 12). LEACE is marginally more aggressive on most models, as expected for the optimal eraser, but the differences are small and directionally consistent. For ZPVE ($\rho = 0.6$), the composition ceiling is high ($R_{\text{comp}}^2 = 0.70$), leaving a thin residual where small absolute differences swap adjacent ranks.

This convergence has a simple explanation. The linear composition subspace is low-rank: $k = 6$ features in $d = 128$ – 1008 dimensional representation spaces. When the concept subspace is this much smaller than the ambient dimension, OLS already captures it nearly completely, leaving little room for the optimal eraser to improve. This means CPD’s simplicity comes at no practical cost relative to more sophisticated erasure methods for composition removal in molecular representations.

5.5 Random Subspace Control

To confirm that CPD removes composition-specific information rather than arbitrary variance, we replace \mathbf{Z} with random matrices of the same dimensionality ($n \times 6$) and measure the z -score of the actual R_{geom}^2 against the null distribution.

All z -scores fall between -163 and -438 . The actual composition projection removes far more predictive variance than any random six-dimensional subspace, confirming that CPD targets a specific and meaningful signal rather than performing generic dimensionality reduction.

5.6 PCA Dimensionality Matching

The models in our study produce representations of varying dimensionality, from 128 (SchNet, PaiNN) to 1008 (ANI-2x). Higher-dimensional representations could in principle retain more information after projection simply because they have more capacity. To control for this, we project all representations to 128 dimensions via PCA before applying CPD. The gradient is preserved, confirming that the ranking reflects representation quality rather than dimensionality (Table 14).

5.7 Summary

Across all checks, we test seven models on four properties under twelve methodological alternatives, producing several hundred individual R^2 comparisons. Rather than applying formal multiple comparison corrections (which assume independent tests), we note that the relevant quantity is *rank preservation*, not significance of individual R^2 values. Spearman ρ is computed on the model ordering, not on individual scores, and a single $\rho = 1.0$ under a given check is itself a single test. Of the twelve rank comparisons, eleven yield $\rho = 1.0$ and one yields $\rho = 0.943$ with the deviation attributable to a single adjacent swap within overlapping error bars.

Taken together, these checks establish three things. First, the gradient is not an artifact of any particular analytical decision: it survives changes to the projection method, the composition features, and the erasure algorithm. Second, CPD is both sufficient and specific: it matches the theoretically optimal eraser (LEACE, $\rho = 1.0$) and removes far more signal than random baselines ($z < -163$). Third, the gradient reflects representation content rather than representation size, as confirmed by PCA dimensionality matching and by the isomer benchmark, which validates CPD through an entirely independent evaluation paradigm. The consistency of these results across such varied perturbations suggests the linear accessibility gradient is a stable, measurable property of the representations themselves.

6 Discussion

6.1 What the Three-Factor Story Means for Practitioners

The dominant role of task alignment has a direct practical implication: when selecting a pre-trained molecular encoder for a downstream property, the training objective matters more than the architecture. An equivariant model pretrained on energies is not automatically a better starting point than an invariant model trained on the same objective. If the downstream target is geometry-sensitive (electronic properties, reactivity, spectroscopic observables), a model trained on a geometry-sensitive objective will provide representations where the relevant signal is already linearly accessible, reducing the burden on the downstream predictor.

Data diversity offers a partial escape from this constraint. MACE pretrained on MPTraj scores 0.364 despite never seeing HOMO-LUMO gap labels, substantially above QM9-only energy models (0.08–0.26). This suggests that large-scale pretraining on diverse structures creates representations with broadly accessible geometric information, even for properties outside the training distribution. For practitioners choosing between a small task-specific model and a large general-purpose foundation model, our results suggest the foundation model’s diversity advantage may partially compensate for objective misalignment, though it does not eliminate it.

Equivariance matters, but conditionally. The practical recommendation is not “use equivariant models” but rather “use equivariant models *with an aligned training objective*.” The combination produces the highest geometric accessibility in our study (PaiNN at 0.533). Either ingredient alone is insufficient.

6.2 Why Does Task Alignment Dominate?

We offer an explanation grounded in the variance structure of the probing problem. For a target property y , let $R_{\text{comp}}^2(y)$ denote the fraction of variance in y explained by composition alone. The remaining fraction, $1 - R_{\text{comp}}^2(y)$, is the *non-compositional variance budget*: the maximum possible R_{geom}^2 under standard CPD. We can state this as a testable prediction:

$$R_{\text{geom}}^2(y) \leq 1 - R_{\text{comp}}^2(y), \quad (2)$$

and the width of the gradient across models for target y is bounded by this ceiling. For targets where composition explains most of the variance, the gradient must compress; for targets where it explains little, the gradient can spread.

Our data is consistent with this prediction across all four properties:

Property	R_{comp}^2	Budget ($1 - R_{\text{comp}}^2$)	Observed spread
HOMO-LUMO gap	0.389	0.611	0.452 (74% of budget)
Dipole moment	0.199	0.801	0.245 (31% of budget)
ZPVE	0.702	0.298	0.118 (40% of budget)
Polarizability	0.868	0.132	0.046 (35% of budget)

The gradient is widest for HOMO-LUMO gap, where the non-compositional budget is largest, and narrowest for polarizability, where it is smallest. The HOMO-LUMO gap gradient also fills the largest fraction of its budget (74%), consistent with the fact that two models in our set (PaiNN, ViSNet) were trained directly on this target. Task alignment creates gradient pressure to encode geometric distinctions in linearly accessible directions; a target dominated by composition creates weaker pressure because the geometric correction is smaller in magnitude.

A formal treatment connecting gradient width to the non-compositional budget as a function of training objective, architecture, and data distribution is a natural direction for future theoretical work. Equation 2 provides the upper bound; characterizing the *lower* bound (what prevents a model from filling its budget) would require modeling the interaction between training dynamics and representation geometry.

6.3 Information Routing and Architectural Inductive Bias

The finding that MACE routes scalar properties through $L=0$ channels and vector properties through $L=1$ channels, while ViSNet does not, points to a qualitative difference in how these architectures use equivariance.

MACE constructs messages via tensor products of spherical harmonics, producing features at each layer that are explicitly tagged by their angular momentum order L . Concretely, a MACE layer outputs a vector of the form $(\mathbf{h}^{L=0}, \mathbf{h}^{L=1}, \mathbf{h}^{L=2}, \dots)$ where each block transforms as the corresponding irreducible representation of $\text{SO}(3)$. This tagging is maintained from input through to the final `descriptors_final` layer, creating channels with well-defined transformation properties that persist in the output representation.

ViSNet maintains scalar and vector streams during message passing but computes geometric interactions at runtime (via vector projections and scalar-vector coupling) rather than maintaining a persistent irreducible decomposition. The result is that ViSNet’s equivariant structure benefits internal computation but does not produce externally readable routing in the final representation, as evidenced by its vector stream carrying nearly zero linearly extractable information ($R^2 = 0.018$).

This distinction has implications for interpretability. If a downstream application requires understanding which geometric features drive a prediction, architectures with persistent irreducible representation channels offer a structured decomposition that can be probed channel by channel. The Materials Project results (Section 4.6) show that MACE’s depth profile increases monotonically to the final layer for all properties, consistent with progressive refinement through persistent channels, while SevenNet and CHGNet show information loss in deep layers.

6.4 Linear vs. Nonlinear Accessibility: The ANI-2x Case

The linear accessibility gradient measures one specific kind of organization: whether geometric information can be extracted by a linear probe after linear composition removal. A low R_{geom}^2 does not mean geometric information is absent; it means the information is not arranged in a linearly readable form.

ANI-2x illustrates this sharply. Under CPD with Ridge probing, ANI-2x scores $R_{\text{geom}}^2 = 0.331$ for HOMO-LUMO gap, placing it in the middle of the energy-trained cluster. But when the linear Ridge probe is replaced with a multilayer perceptron (two hidden layers, 256 units each), the same geometric residual yields $R^2 = 0.784$. The gap between these two numbers ($\Delta = 0.453$) is the largest linear-nonlinear discrepancy in our model set.

This means ANI-2x encodes rich geometric information that is present but nonlinearly entangled with other features in the residual subspace. The same information that PaiNN makes linearly accessible, ANI-2x makes available only through nonlinear readout. Both models “know” the geometry; they differ in how they organize that knowledge.

This finding has two implications. First, the linear accessibility gradient is not a proxy for total information content. It measures representation *organization*, not representation *quality*. A model at the bottom of the gradient (like MACE QM9 at 0.081) may still encode useful geometric features that a nonlinear downstream model can exploit. Second, the practical value of linear disentanglement depends on the downstream consumer. If the consumer is a simple linear head (as in few-shot transfer or interpretable probing), linearly disentangled representations like PaiNN’s offer a large advantage. If the consumer is a deep network with its own nonlinear capacity, the advantage shrinks.

6.5 Connection to Representation Learning Theory

CPD measures a specific form of disentanglement: linear accessibility of one known factor (geometry) after linear removal of another (composition). This is narrower than the general disentanglement studied by Higgins et al. (2017) and Locatello et al. (2019), which seeks to discover and separate unknown latent factors. Our setting is simpler because the factors are known and one of them (composition) is directly observable.

This simplicity is also a strength. Locatello et al. (2019) showed that unsupervised disentanglement requires inductive biases but left open the question of which biases help. In our setting, we can identify three specific biases that matter: task alignment (a supervised bias from the training objective), equivariance (an architectural bias from the network design), and data diversity (a distributional bias from the training set). The finding that a supervised bias dominates over an architectural bias resonates with the broader lesson from Locatello et al. (2019): without appropriate supervision, structural inductive biases alone do not guarantee organized representations.

7 Limitations

Dataset scope. CPD results in this paper cover QM9 (134,000 small organic molecules, up to 9 heavy atoms, 5 elements) and Materials Project crystals (periodic inorganic structures with diverse compositions). This spans two important chemical domains, but does not include larger drug-like molecules (GEOM-Drugs, QM7-X), surface chemistry (OC20/OC22), or protein-ligand interactions. The MP crystals analysis uses three models and has not undergone the same twelve-check robustness battery as the QM9 results. Whether the three-factor story holds quantitatively in these additional domains remains an open question.

Frozen representations only. CPD probes frozen, pretrained representations. It does not measure what a model *could* learn under finetuning, only what it has already encoded. A model with low R_{geom}^2 might still achieve high downstream accuracy after finetuning if the geometric information exists in a nonlinearly accessible form. Our ANI-2x results illustrate this: under linear probing, ANI-2x scores moderately (0.331), but MLP probes recover substantially more ($R^2 = 0.784$ in earlier experiments with global CPD), suggesting rich geometric information is present but nonlinearly entangled.

Linear decomposition. CPD removes only the *linear* relationship between composition and representation. Nonlinear functions of composition that the model has learned to encode will remain in the residual and be attributed to “geometry.” This is a known property of the method and is the reason GBT probes are inflated (Section 4.3). The LEACE validation (Section 5.4) confirms that the linear erasure is sufficient for ranking models, but it does not guarantee that all composition signal has been removed in an absolute sense.

Causal claims. We report associations between model attributes (architecture, training objective, data) and R_{geom}^2 , not causal effects. The MACE ablation holds architecture constant and varies training, providing evidence for a causal role of training conditions. But the cross-architecture comparisons (e.g., PaiNN vs. SchNet) are confounded by differences in implementation, hyperparameters, and parameter count. We use “shapes” rather than “causes” throughout to reflect this epistemic status.

Factorial coverage. The PaiNN and MACE ablations each provide a within-architecture test of task alignment, and both show large effects ($\Delta = 0.223$ and 0.338 respectively). We do not have the complementary ablation for SchNet (trained on HOMO-LUMO gap), which would extend the test to an invariant architecture. The MACE pretrained vs. QM9-only comparison varies both data and objective simultaneously, making it less clean than the PaiNN or MACE-HL ablations for isolating task alignment alone.

DimeNet++ convergence. DimeNet++ was trained for only 30 epochs and achieves the lowest R_{full}^2 (0.617), suggesting incomplete convergence. Its position at the bottom of the energy-trained invariant group may partly reflect undertrained representations rather than an architectural limitation.

Sample size. All primary probing experiments use 2,000 molecules from QM9 (1.5% of the dataset). The sample efficiency analysis (Section 4.5) shows the ranking is stable down to $N = 500$ ($\rho = 1.0$) and largely stable at $N = 50$ ($\rho = 0.964$), but we have not tested whether additional models would interpolate smoothly into the ranking or whether the gradient structure changes at substantially larger sample sizes (e.g., $N = 10,000$ or full QM9).

8 Broader Impact

This work contributes to the understanding of learned representations in molecular property prediction. The primary societal relevance is indirect: better understanding of what molecular models encode may improve model selection for drug discovery, catalyst design, and materials screening, accelerating progress in healthcare and clean energy applications.

The GBT inflation finding (Section 4.3) has methodological implications beyond molecular modeling. Representational probing is widely used in NLP (Conneau et al., 2018; Hewitt & Manning, 2019) and computer vision (Alain & Bengio, 2017), and concept erasure methods like LEACE (Belrose et al., 2023) are increasingly applied to fairness and bias auditing. Our demonstration that nonlinear probes recover $R^2 = 0.68$ to 0.95 on a target that has been linearly erased is a cautionary result for any field that uses residualization-based probing to draw conclusions about what information a model has or has not encoded.

We do not foresee direct negative societal consequences from this work. CPD is an analysis tool, not a generative model, and does not produce novel molecules or materials. The datasets used (QM9) are publicly available and contain no private or sensitive information.

9 Reproducibility Statement

All experiments use publicly available data (QM9 via PyTorch Geometric) and publicly released model checkpoints where available (MACE pretrained, ANI-2x, SchNet, DimeNet++). The PaiNN model was trained from scratch using a self-contained implementation; training details and the full configuration appear in Appendix B. MACE QM9 variants were trained using the public MACE codebase with configurations specified in Appendix C.

The CPD implementation is straightforward (Equation 1): OLS projection within each cross-validation fold followed by Ridge regression probing. All hyperparameters are specified in Section 3.3: 20 log-spaced Ridge alphas from 10^{-3} to 10^6 , 5-fold CV, 30 seeds with deterministic seed formula (`seed × 100 + 7`), and fixed molecule selection via `np.random.RandomState(42)`.

References

- Alain, G. and Bengio, Y. Understanding intermediate layers using linear classifier probes. In *ICLR Workshop*, 2017.
- Batatia, I., Kovács, D. P., Simm, G. N., Ortner, C., and Csányi, G. MACE: Higher order equivariant message passing neural networks for fast and accurate force fields. In *NeurIPS*, 2022.
- Batatia, I., Batzner, S., Kovács, D. P., Musaelian, A., Simm, G. N. C., Drautz, R., Ortner, C., Kozinsky, B., and Csányi, G. The design space of E(3)-equivariant atom-centered interatomic potentials. *arXiv:2205.06643*, 2022.
- Belrose, N., Schneider-Joseph, D., Ravfogel, S., Cotterell, R., Raff, E., and Biderman, S. LEACE: Perfect linear concept erasure in closed form. In *NeurIPS*, 2023.
- Bengio, Y., Courville, A., and Vincent, P. Representation learning: A review and new perspectives. *IEEE TPAMI*, 35(8):1798–1828, 2013.
- Conneau, A., Kruszewski, G., Lample, G., Barrault, L., and Baroni, M. What you can cram into a single \mathbb{R}^d vector: Probing sentence embeddings for linguistic properties. In *ACL*, 2018.
- Devereux, C., Smith, J. S., Huddleston, K. K., Barros, K., Zubatyuk, R., Isayev, O., and Roitberg, A. E. Extending the applicability of the ANI deep learning molecular potential to sulfur and halogens. *J. Chem. Theory Comput.*, 16(7):4192–4202, 2020.
- Hewitt, J. and Liang, P. Designing and interpreting probes with control tasks. In *EMNLP*, 2019.

- Hewitt, J. and Manning, C. D. A structural probe for finding syntax in word representations. In *NAACL*, 2019.
- Higgins, I., Matthey, L., Pal, A., Burgess, C., Glorot, X., Botvinick, M., Mohamed, S., and Lerchner, A. β -VAE: Learning basic visual concepts with a constrained variational framework. In *ICLR*, 2017.
- Huh, M., Cheung, B., Wang, T., and Isola, P. The platonic representation hypothesis. In *ICML*, 2024.
- Klicpera, J., Giri, S., Margraf, J. T., and Günnemann, S. Fast and uncertainty-aware directional message passing for non-equilibrium molecules. In *NeurIPS ML for Molecules Workshop*, 2020.
- Kornblith, S., Norouzi, M., Lee, H., and Hinton, G. E. Similarity of neural network representations revisited. In *ICML*, 2019.
- Locatello, F., Bauer, S., Lucic, M., Rätsch, G., Gelly, S., Schölkopf, B., and Bachem, O. Challenging common assumptions in the unsupervised learning of disentangled representations. In *ICML*, 2019.
- Schütt, K. T., Kindermans, P.-J., Sauceda, H. E., Chmiela, S., Tkatchenko, A., and Müller, K.-R. SchNet: A continuous-filter convolutional neural network for modeling quantum interactions. *NeurIPS*, 2017.
- Schütt, K. T., Unke, O. T., and Gastegger, M. Equivariant message passing for the prediction of tensorial properties and molecular spectra. In *ICML*, 2021.
- Wang, Y., Wang, T., Li, S., et al. ViSNet: an equivariant geometry-enhanced graph neural network with vector-scalar interactive message passing for molecules. *Nature Communications*, 15:313, 2024.
- Wang, A. Y.-T., Kauwe, S. K., Murdock, R. J., and Sparks, T. D. Compositionally restricted attention-based network for materials property predictions. *npj Computational Materials*, 7:77, 2021.
- Ward, L., Dunn, A., Faghaninia, A., et al. Matminer: An open source toolkit for materials data mining. *Computational Materials Science*, 152:60–69, 2018.

A Robustness Tables

B PaiNN Training Details

PaiNN was trained from a self-contained implementation because the PyTorch Geometric built-in PaiNN class was unavailable in our environment. The architecture uses 6 message-passing layers with 128 hidden dimensions and a radial cutoff of 5.0 Å, totaling 1.16M parameters. Representations were extracted from the `scalar_out` layer (128 dimensions) after mean pooling over atoms.

Two variants were trained with identical architecture:

- **PaiNN (HOMO-LUMO)**: 30 epochs on QM9 HOMO-LUMO gap with the Adam optimizer, achieving a test RMSE of 81.8 meV.

Table 9: Fold-wise vs. global CPD on HOMO-LUMO gap (30-seed). Global QR over-removes geometric signal by projecting out a wider subspace informed by test-fold composition vectors.

Model	Fold-wise	Global	Δ
ViSNet	0.513	0.444	+0.069
MACE pretrained	0.364	0.295	+0.047
ANI-2x	0.331	0.276	+0.055
SchNet	0.262	0.238	+0.024
DimeNet++	0.240	0.176	+0.065
MACE QM9 97ep	0.101	0.090	+0.011

Table 10: Frisch-Waugh-Lovell partial R^2 on HOMO-LUMO gap. FWL residualizes both \mathbf{X} and y , measuring the fraction of non-compositional target variance explained by the geometric residual.

Model	Standard R_{geom}^2	FWL Partial R^2	Δ
ViSNet	0.444	0.826	+0.383
ANI-2x	0.276	0.691	+0.415
MACE pretrained	0.295	0.644	+0.349
SchNet	0.238	0.538	+0.300
DimeNet++	0.176	0.440	+0.264
MACE QM9 97ep	0.090	0.167	+0.076

Note: Standard R_{geom}^2 here uses global CPD (the FWL experiment predates the fold-wise correction).

- **PaiNN-energy**: 30 epochs on QM9 energy (U_0) with the same optimizer and learning rate schedule. Test RMSE of approximately 30 eV (note: this is poor for U_0 , which has a large dynamic range, but the experiment isolates the effect of training objective on representation structure rather than prediction quality).

C MACE QM9 Training Details

All MACE QM9 variants use the public MACE codebase with identical architecture: ScaleShift-MACE with 128 scalar ($L=0$) + 128 vector ($L=1$) channels, $\ell_{\text{max}} = 2$, correlation order 3, totaling 727,824 parameters. Three variants were trained:

- **MACE-HL**: 30 epochs on QM9 HOMO-LUMO gap (mapped as the “energy” key for the MACE training pipeline). Test RMSE: 25.8 meV. Representations extracted from `descriptors_final` (640 dims).
- **MACE QM9 97ep**: 97 epochs on QM9 energy (U_0). Representations extracted from `node_feats_out` (640 dims).
- **MACE QM9 30ep**: 30 epochs on QM9 energy (U_0), same configuration. Representations extracted from the same layer.

MACE pretrained uses the publicly released checkpoint trained on MPTraj (millions of structures, energy + forces). Representations were extracted from `descriptors_final` (256 dims).

Table 11: Composition feature sensitivity on HOMO-LUMO gap (R_{geom}^2). Z1: element fractions + normalized atom count (default). Z2: raw element counts + raw atom count. Z3: element fractions only, no atom count. Z4: binary element presence + normalized atom count. Spearman $\rho = 1.000$ for all pairwise comparisons.

Model	Z1 (default)	Z2 (raw)	Z3 (frac only)	Z4 (binary)
ViSNet	0.467	0.448	0.466	0.527
MACE pretrained	0.364	0.325	0.362	0.430
ANI-2x	0.331	0.310	0.331	0.402
SchNet	0.262	0.253	0.266	0.336
DimeNet++	0.240	0.211	0.238	0.292
MACE QM9 97ep	0.101	0.108	0.099	0.119

Table 12: CPD vs. LEACE concept erasure on HOMO-LUMO gap (R_{geom}^2). LEACE finds the theoretically optimal linear projection for removing composition. Mean $|\Delta| = 0.012$. Spearman $\rho = 1.000$.

Model	CPD	LEACE	Δ
ViSNet	0.467	0.472	+0.005
MACE pretrained	0.364	0.362	-0.002
ANI-2x	0.331	0.319	-0.012
SchNet	0.262	0.280	+0.018
DimeNet++	0.240	0.243	+0.003
MACE QM9 97ep	0.101	0.068	-0.033

D Notation

Table 15 summarizes the notation used throughout the paper.

E Experimental Constants

Table 16 lists all fixed values used across experiments. These are sufficient, together with the code release, to reproduce all results reported in the paper.

F QM9 Depth Profiles (Fold-Wise CPD)

Layer-by-layer R_{geom}^2 for HOMO-LUMO gap on QM9, using fold-wise CPD (30-seed \times 5-fold).

MACE pretrained. Two-stage build with tensor product jumps. Peaks at `descriptors_final` (0.364). The $L=1$ vector channel at `interaction_0` carries $R_{\text{geom}}^2 = -0.003$, confirming that early vector features contain no linearly accessible geometric information for scalar properties.

Layer	Dim	R_{full}^2	R_{geom}^2
interaction_0	2048	0.695	0.221
product_0	512	0.757	0.296
interaction_1	2048	0.703	0.324
product_1	128	0.726	0.329
descriptors_final	256	0.786	0.364

Table 13: Structural isomer distance correlations. Spearman correlation between pairwise \mathbf{X}_{geom} distances and HOMO-LUMO gap differences for 38,784 isomer pairs. All \mathbf{X}_{comp} correlations are near zero ($|\rho| < 0.005$, $p > 0.38$), confirming CPD isolates geometric from compositional information.

Model	Geom ρ	Geom p	Comp ρ	Comp p
PaiNN	0.768	0.00	-0.004	0.385
ViSNet	0.458	0.00	-0.004	0.390
MACE pretrained	0.234	0.00	-0.004	0.403
ANI-2x	0.136	7.2e-160	-0.004	0.406
MACE QM9 97ep	0.138	6.4e-165	-0.004	0.392
DimeNet++	0.089	1.8e-68	0.001	0.802
SchNet	0.077	2.0e-51	0.004	0.449

Table 14: PCA dimensionality matching. All representations projected to 128 dimensions via PCA before applying CPD. The ranking is preserved, confirming the gradient reflects representation quality rather than dimensionality.

Model	Original dims	Original R^2_{geom}
PaiNN	128	0.533
ViSNet	128	0.513
MACE pretrained	256	0.364
ANI-2x	1008	0.331
SchNet	128	0.262
DimeNet++	128	0.240
MACE QM9 97ep	640	0.101
MACE QM9 30ep	640	0.081

Models at 128 dims are unaffected by PCA. Ranking preserved after projection.

SchNet. Peaks early at interaction_0 (0.270), declines mid-network, partially recovers. Unlike MACE, deeper layers do not monotonically improve geometric accessibility.

Layer	Dim	R^2_{full}	R^2_{geom}
embedding	128	0.390	-0.003
interaction_0	128	0.688	0.270
interaction_1	128	0.682	0.268
interaction_2	128	0.692	0.262
interaction_3	128	0.566	0.196
interaction_4	128	0.639	0.210
interaction_5	128	0.677	0.246

DimeNet++. Steady build through interaction blocks. Peaks at interaction_3 (0.240). Output blocks (scalar predictions) carry no signal.

Layer	Dim	R^2_{full}	R^2_{geom}
emb	128	0.362	0.061
interaction_0	128	0.606	0.222
interaction_1	128	0.502	0.198
interaction_2	128	0.585	0.225
interaction_3	128	0.617	0.240

Table 15: Summary of notation.

Symbol	Type	Definition
<i>Data and representations</i>		
n	scalar	Number of molecules in the probe set
d	scalar	Dimensionality of model representation
k	scalar	Number of composition features (default 6)
$\mathbf{X} \in \mathbb{R}^{n \times d}$	matrix	Molecular representations from frozen model
$\mathbf{Z} \in \mathbb{R}^{n \times k}$	matrix	Composition feature matrix
$\mathbf{z} \in \mathbb{R}^k$	vector	Composition features for a single molecule
y	scalar	Target property value
<i>CPD decomposition</i>		
$\hat{\beta} \in \mathbb{R}^{k \times d}$	matrix	OLS coefficients: $(\mathbf{Z}^\top \mathbf{Z})^{-1} \mathbf{Z}^\top \mathbf{X}$
\mathbf{X}_{geom}	matrix	Geometric residual: $\mathbf{X} - \mathbf{Z} \hat{\beta}$
\mathbf{X}_{comp}	matrix	Compositional component: $\mathbf{Z} \hat{\beta}$
\mathbf{Q}, \mathbf{R}	matrices	QR decomposition of \mathbf{Z} (equivalent formulation)
<i>Evaluation metrics</i>		
R_{full}^2	scalar	Ridge R^2 on full (unprojected) representation \mathbf{X}
R_{geom}^2	scalar	Ridge R^2 on geometric residual \mathbf{X}_{geom}
R_{comp}^2	scalar	Ridge R^2 on compositional component \mathbf{X}_{comp}
ρ	scalar	Spearman rank correlation coefficient
Δ	scalar	Difference between two conditions
Δ_{best}	scalar	Best model R^2 minus composition baseline R^2
<i>Equivariant channels</i>		
L	integer	Angular momentum order of irreducible representation
$L=0$	—	Scalar (rotationally invariant) channel
$L=1$	—	Vector (rotates with coordinate frame) channel
ℓ_{max}	integer	Maximum angular momentum order in MACE
<i>Composition feature specifications</i>		
Z1	—	Element fractions + standardized atom count (default)
Z2	—	Raw element counts + raw atom count
Z3	—	Element fractions only (no atom count)
Z4	—	Binary element presence + standardized atom count

ViSNet. Monotonic increase through all layers, peaking at the task-specific output layer (`output_network_0_out0`, $R^2 = 0.504$). This is higher than anything in the backbone (max 0.467 at layer 5), illustrating task alignment operating at the readout level: the output network, trained for property prediction, further refines geometric accessibility beyond what message passing alone achieves. The `out1` channel (dim=3) is the dead vector stream ($R^2 = 0.012$).

Layer	Dim	R_{full}^2	R_{geom}^2
vis_mp_layers_0	128	0.784	0.361
vis_mp_layers_1	128	0.766	0.376
vis_mp_layers_2	128	0.822	0.407
vis_mp_layers_3	128	0.841	0.431
vis_mp_layers_4	128	0.848	0.439
vis_mp_layers_5	128	0.877	0.467
output_network_0_out0	64	0.914	0.504
output_network_0_out1	3	0.055	0.012

G Nonlinear Encoding (Ridge vs. MLP)

To assess how much geometric information exists in nonlinearly accessible form, we replace Ridge probes with MLPs (2 hidden layers of 256 and 128 units, early stopping, 10 seeds \times 5 folds) on the same geometric residual \mathbf{X}_{geom} .

MACE QM9 jumps from last place under Ridge (0.100) to fourth under MLP (0.439), a $4.4\times$ increase. Its tensor product architecture encodes rich geometric structure in a form that requires nonlinear readout. This reinforces the distinction between representation *quality* and representation *organization* discussed in Section 6.

H Intercept Diagnostic

To verify the sensitivity of CPD to intercept handling, we run a 2×2 design: {global, fold-wise} \times {fit_intercept=True, False}.

All results in the paper use fold-wise CPD with fit_intercept=True (rightmost column).

I v1 Discrepancy Resolution

An earlier version of this work (arXiv:2603.03155 v1) reported $R_{\text{geom}}^2 \approx 0.78$ for MACE pretrained. The present paper reports $R_{\text{geom}}^2 = 0.364$ (fold-wise) or 0.295 (global) for the same checkpoint and dataset. The discrepancy is resolved by examining the v1 result files:

v1 field	Value
R2_full	0.787
R2_cpd_geom	0.292
R2_ridge_resid	0.783
R2_cpd_comp	0.392

v1 reported R2_ridge_resid (a two-stage procedure that residualizes the *target* against composition, then probes the *full, unprojected* representation \mathbf{X}) instead of R2_cpd_geom (which residualizes the *representation*). Since composition was not removed from \mathbf{X} , the probe could still exploit compositional signal, producing $R^2 \approx R_{\text{full}}^2$. The correct CPD value (R2_cpd_geom = 0.292) matches the present paper’s global CPD result (0.295) within rounding. All results in this paper use CPD (representation residualization), not target residualization.

J CKA Representational Similarity

To understand whether models with similar R_{geom}^2 scores also produce similar internal representations, we compute Centered Kernel Alignment (CKA; Kornblith et al. 2019) between all model pairs. CKA measures the similarity of two representation matrices independent of their dimensionality, producing a value between 0 (orthogonal) and 1 (identical up to linear transformation).

We compute CKA on Materials Project crystal representations for four models: MACE, CHGNet, SevenNet, and ORB v2 (a transformer-based model). The analysis reveals two findings.

First, MACE and CHGNet share high representational similarity at their final layers (CKA > 0.8), consistent with both being message-passing models trained on similar energy/force objectives on overlapping crystal datasets. Their probe-level performance is also similar (Table 7).

Second, ORB v2 diverges from all three message-passing models (CKA < 0.4 at final layers), consistent with its transformer-based architecture producing qualitatively different representation geometry. Despite this divergence, ORB v2 and MACE can reach comparable R^2 values on some properties, suggesting that different internal representations can support similar levels of linear geometric accessibility. This resonates with the Platonic Representation Hypothesis (Huh et al., 2024) at the functional level (similar readout) while contradicting it at the representational level (different internal geometry).

CKA analysis is complementary to CPD: where CPD measures what information is accessible, CKA measures how the representation space is organized globally. A full integration of these perspectives, examining whether CKA similarity predicts CPD similarity, is left to future work.

K SHAP Feature Importance Stability

To probe which dimensions of the representation drive R_{geom}^2 , we compute SHAP (SHapley Additive exPlanations) values for the Ridge probe on \mathbf{X}_{geom} . SHAP assigns each feature dimension an importance score reflecting its marginal contribution to the prediction. We assess stability by bootstrapping: we resample the 2,000-molecule probe set 100 times and compute the Spearman correlation between SHAP importance rankings across bootstrap halves.

MACE shows moderate SHAP stability (Spearman $\rho = 0.54$ between bootstrap halves), indicating that many dimensions contribute to the prediction and their relative ranking is sensitive to the sample. ANI-2x shows higher stability ($\rho = 0.75$), consistent with a smaller number of dimensions carrying the geometric signal. This difference aligns with the architectural contrast: MACE distributes information across 256 equivariant channels (128 scalar + 128 vector), while ANI-2x concentrates information in handcrafted symmetry function outputs where fewer features dominate.

The moderate bootstrap stability for MACE suggests caution in interpreting individual feature importances. The overall R_{geom}^2 is highly stable across seeds (standard deviation 0.007), but the specific features driving that score vary with the sample. This is expected for high-dimensional Ridge regression with correlated features and does not undermine the aggregate CPD results.

Table 16: Fixed experimental constants.

Constant	Description	Value
<i>Probe set construction</i>		
n	Number of QM9 molecules sampled	2,000
Molecule seed	<code>np.random.RandomState(seed)</code>	42
QM9 elements	Elements present in dataset	C, H, N, O, F
<i>Cross-validation</i>		
K	Number of CV folds	5
S	Number of random seeds	30
Seed formula	<code>random_state</code> per fold	<code>seed × 100 + 7</code>
<i>Ridge regression</i>		
$ \mathcal{A} $	Number of regularization values	20
α_{\min}	Minimum regularization	10^{-3}
α_{\max}	Maximum regularization	10^6
α spacing	Log-spaced between α_{\min} and α_{\max}	—
Intercept	<code>fit_intercept</code>	True
<i>Threading</i>		
<code>OMP_NUM_THREADS</code>	OpenMP threads	4
<code>MKL_NUM_THREADS</code>	MKL threads	4
<code>OPENBLAS_NUM_THREADS</code>	OpenBLAS threads	4
<i>Composition features (Z1 default)</i>		
k	Number of composition features	6
Features 1–5	Element fractions (C, H, N, O, F)	n_e/n_{total}
Feature 6	Atom count	z-scored
<i>Structural isomer benchmark</i>		
Isomer groups	Groups within 2,000-molecule set	150
Isomer molecules	Molecules in isomer groups	1,931
Isomer pairs	Total pairwise comparisons	38,784
Classifier	Isomer ordering probe	LogisticRegressionCV
<i>QM9 target property indices</i>		
HOMO-LUMO gap	Index in QM9 label vector	4
Dipole moment	Index in QM9 label vector	0
Polarizability	Index in QM9 label vector	1
ZPVE	Index in QM9 label vector	11
<i>Sample efficiency</i>		
N values	Sample sizes tested	50, 100, 200, 500, 1K, 2K

Table 17: Linear vs. nonlinear probing on \mathbf{X}_{geom} for HOMO-LUMO gap. “NL Gap” is the difference between MLP and Ridge R^2 , measuring how much geometric information is nonlinearly but not linearly accessible. ANI-2x was PCA-projected to 128 dimensions (99.94% variance retained) to prevent MLP divergence on 1008-dimensional input.

Model	Ridge	MLP	NL Gap	Category
PaiNN	0.534	0.833	+0.299	High linear + high NL
ViSNet	0.468	0.789	+0.321	High linear + high NL
MACE pretrained	0.363	0.753	+0.390	Moderate + high NL
ANI-2x (PCA)	0.327	0.607	+0.279	Moderate all
MACE QM9	0.100	0.439	+0.339	Low linear + moderate NL
SchNet	0.260	0.470	+0.210	Moderate all
DimeNet++	0.241	0.345	+0.104	Low all

Table 18: Intercept diagnostic on HOMO-LUMO gap. Without intercept, Ridge regression produces catastrophic $R^2 \approx -28$ because the residualized \mathbf{X}_{geom} has near-zero mean and Ridge without intercept cannot model the target’s mean.

Model	Glob+noInt	Glob+Int	FW+noInt	FW+Int
MACE pre.	-27.89	0.295	-27.82	0.364
ViSNet	-27.77	0.444	-27.67	0.467
SchNet	-27.95	0.238	-27.92	0.262
ANI-2x	-27.94	0.276	-27.91	0.331